Supplement of Atmos. Chem. Phys. Discuss., 14, 23681–23709, 2014
http://www.atmos-chem-phys-discuss.net/14/23681/2014/
doi:10.5194/acpd-14-23681-2014-supplement

Atmospheric Chemistry and Physics Discussions
Open Access

Supplement of

The potential for regional-scale bias in top-down CO_2 flux estimates due to atmospheric transport errors

S. M. Miller et al.

Correspondence to: S. M. Miller (scot.m.miller@gmail.com)

Supplement of Atmos. Chem. Phys. Discuss., 14, 23681–23709, 2014
http://www.atmos-chem-phys-discuss.net/14/23681/2014/
doi:10.5194/acpd-14-23681-2014-supplement

Atmospheric Chemistry and Physics
Discussions
Open Access

Supplement of

The potential for regional-scale bias in top-down CO_2 flux estimates due to atmospheric transport errors

S. M. Miller et al.

Correspondence to: S. M. Miller (scot.m.miller@gmail.com)

S1 The meteorological model-data assimilation framework

This section of the supplement describes the Local Ensemble Kalman Filter (LETKF) in greater detail. Many of the equations listed below are abbreviated versions of those detailed in Hunt et al. (2004), Desroziers et al. (2005), Hunt et al. (2007), Li et al. (2009), and Miyoshi (2011). For a mathematical derivation of either the meteorology optimization or covariance matrix estimation within LETKF, refer to any of those studies.

The model–data assimilation system (abbreviated CAM–LETKF) can be summarized in a number of steps. First, we create an initial condition for modeled meteorology, in this case using NCEP–DOE AMIP-II reanalysis (Kanamitsu et al., 2002). We generate a set of small perturbations to the initial conditions and use these perturbations to create a set of k initial conditions that are all slightly different. In this case, we set $k = 64$ (as in Liu et al., 2011, 2012). This choice represents a compromise between thorough statistical sampling and computational considerations: a very large k will exhaustively sample the model uncertainties. However, k CAM–CLM realizations require $4k$ computer cores, so a very large k would also become computationally prohibitive.

Second, we run a 6-hour weather forecast using CAM-CLM for each for the k model initial conditions. The spread of this model ensemble represents our prior uncertainty in the modeled meteorology:

$$\boldsymbol{x}_i \;=\; \bar{\boldsymbol{x}} + \mathbf{X}_i \quad \text{where } i = 1....k \tag{S1}$$

where $\boldsymbol{x}_i$ $(m \times 1)$ is a single model realization, $\bar{\boldsymbol{x}}$ $(m \times 1)$ is the mean of the model ensemble, and $\mathbf{X}_i$ $(m \times k)$ refers to the i^{th} column of the matrix that defines the model ensemble spread. In the main article (e.g., Eq. 1), we defined these variables to refer to all model time steps, collectively. In the supplement, by contrast, we will instead define these variables to refer to the model–data assimilation at a single, 6-hourly time step. In other words, m and n now refer to the model outputs and number of weather observations, respectively, associated with a single model–data assimilation cycle. This redefinition of the variables facilitates a discussion of time-stepping in the remainder of this section.

Third, we calculate a set of k weights such that the weighted average of the realizations best matches the meteorological observations:

$$\bar{\boldsymbol{x}}^a \;=\; \bar{\boldsymbol{x}}^b + \mathbf{X}^b \hat{\boldsymbol{w}} \tag{S2}$$

The superscript b refers to the model state before assimilation and a the model state after data assimilation. The $k \times 1$ vector of weights $(\hat{\boldsymbol{w}})$ are estimated by minimizing a statistical cost function with respect to the meteorological observations (Hunt et al., 2007):

$$J(\boldsymbol{w}) \;=\; (k-1)\boldsymbol{w}^T\boldsymbol{w} + \Big(\boldsymbol{z} - H(\bar{\boldsymbol{x}}^b + \mathbf{X}^b\boldsymbol{w})\Big)^T \mathbf{R}^{-1} \Big(\boldsymbol{z} - H(\bar{\boldsymbol{x}}^b + \mathbf{X}^b\boldsymbol{w})\Big) \tag{S3}$$

In the above equation, $\boldsymbol{z}$ $(n\times 1)$ represents the meteorological observations, and $H()$ is a function or operator that maps the model output to the observations. For example, the function $H()$ may convert the model units to the measurement units or may interpolate the model output to an observation site that lies between multiple model grid boxes. Lastly, the diagonal matrix $\mathbf{R}$ $(n \times n)$ represents the nugget variance, variance in the model–data residuals that is due to measurement errors or meteorological processes too small in scale to be captured by CAM–CLM.

Note that, in practice, we never compute the weights simultaneously for the entire global model output. Rather, we estimate a different set of weights for each model grid box using observations within a certain radius (in this case, within 1500km). As such, the matrices in

Eqs. S2 and S3 represent a subset of the global model output, and the dimensions n and m are small relative to the total number of global observations and model grid boxes, respectively.

The estimated weights ($\hat{\boldsymbol{w}}$) have the following covariance matrix ($k \times k$) (Hunt et al., 2007):

$$\tilde{\mathbf{P}}^a = (k-1)\mathbf{I} + (\mathbf{Y}^b)^T\mathbf{R}^{-1}\mathbf{Y}^b \tag{S4}$$

$$\text{where} \quad H(\bar{\boldsymbol{x}}^b + \mathbf{X}^b\boldsymbol{w}) \approx \bar{\boldsymbol{y}}^b + \mathbf{Y}^b\boldsymbol{w} \tag{S5}$$

Fourth, we generate 64 realizations that collectively represent our posterior uncertainty in the meteorology. Like the best estimate ($\bar{\boldsymbol{x}}^a$), these posterior realizations are also a linear combination of the prior model realizations (Hunt et al., 2007):

$$\boldsymbol{x}_i^a = \bar{\boldsymbol{x}}^a + \mathbf{X}^b\left(\left[(k-1)\tilde{\mathbf{P}}^a\right]^{\frac{1}{2}}\right)_i \tag{S6}$$

where '$\frac{1}{2}$' denotes the symmetric square root of the covariance matrix. The subscript i on the right hand side of the equation refers to individual columns of the matrix.

Fifth, and finally, we adjust the overall model ensemble spread to match the model uncertainties implied by the meteorological observations. We refer to this process as adaptive covariance inflation (e.g., Li et al., 2009; Miyoshi, 2011). Note that this step is new since previous CAM–LETKF studies by Liu et al. (2011) and Liu et al. (2012).

Adaptive inflation operates on the following principle: the ensemble variance and nugget variance should match against the actual model-data residuals (e.g., Li et al., 2009):

$$E\left[\left(\boldsymbol{z} - H(\bar{\boldsymbol{x}}^b)\right)\left(\boldsymbol{z} - H(\bar{\boldsymbol{x}}^b)\right)^T\right] = \mathbf{HPH}^T + \mathbf{R} \tag{S7}$$

$$\text{where} \quad \mathbf{P} = (k-1)^{-1}\mathbf{X}^b(\mathbf{X}^b)^T \tag{S8}$$

In that equation, E denotes the expected value, and the matrix $\mathbf{H}$ ($n \times m$) is a linearization of the function $H()$. In practice, however, these covariance matrices can diverge from the actual residuals (refer to Miyoshi, 2011, for more detail). Therefore, we estimate a scaling factor (α) for the diagonal elements of the covariance matrix $\mathbf{P}$ ($m \times m$). This scaling factor can be estimated by manipulating Eq. S7 as in Li et al. (2009) and Miyoshi (2011):

$$\alpha = \frac{tr\left[\left(\boldsymbol{z} - H(\bar{\boldsymbol{x}}^b)\right)\left(\boldsymbol{z} - H(\bar{\boldsymbol{x}}^b)\right)^T \circ \mathbf{R}^{-1}\right] - n}{tr\left[\mathbf{HPH}^T \circ \mathbf{R}^{-1}\right]} \tag{S9}$$

In this equation, tr refers to the matrix trace, and the symbol $\circ$ indicates element-wise multiplication. The result of Eq. S9 is then weighted against the scaling factor from the previous model time step to produce a final scaling factor estimate (refer to Li et al., 2009; Miyoshi, 2011).

We also estimate the nugget variance ($\sigma^2_{\mathbf{R},j}$) for a given observation type (j) using the model output and observations (Desroziers et al., 2005; Li et al., 2009):

$$\sigma^2_{\mathbf{R},j} = \frac{\left(\boldsymbol{z}_j - H(\bar{\boldsymbol{x}}^a)\right)^T\left(\boldsymbol{z}_j - H(\bar{\boldsymbol{x}}^b)\right)}{n_j} \tag{S10}$$

As with α, the result in Eq. S10 is also weighted against the estimated variance from the previous time step to produce a final variance estimate (Li et al., 2009). Unlike the localized LETKF calculations, we estimate a single nugget variance for the entire globe (for each meteorological observation type). In other words, in Eq. S10, the inputs represent global values for observation type j, not a localized implementation as in previous equations.

After these steps, the model-assimilation cycle begins again with another 6-hour CAM–CLM forecast. The posterior ensemble members ($\boldsymbol{x}_i^a$) become the initial conditions for this next CAM-CLM forecast.

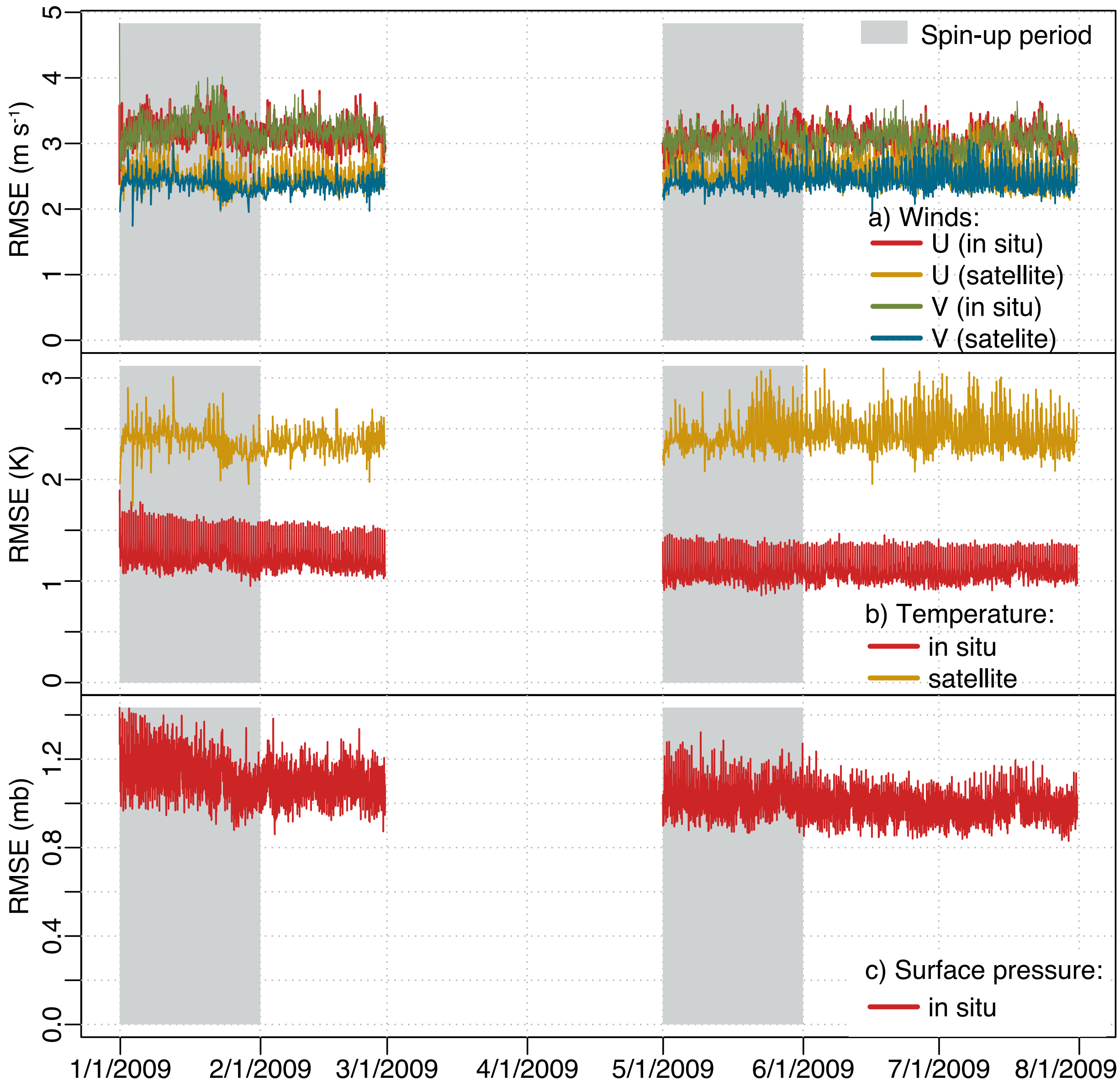

Figure S1: Root mean squared errors for the CAM–LETKF best estimate compared against various meteorological observations (RMSE, $\sqrt{(1/n)\sum(\mathbf{y} - H(\bar{\boldsymbol{x}}^a))^2}$).

S2 CAM–LETKF performance metrics

The paragraphs that follow discuss two different metrics of CAM–LETKF performance: large-scale meteorology model–data comparisons and a more in-depth view of the estimated variances (i.e., the variance inflation and the nugget variance).

First, we examine the meteorology model–data residuals for the model best-guess ($\bar{\boldsymbol{x}}^a$). Figure S1 displays the root mean squared model–measurement error (RMSE, $\sqrt{(1/n)\sum(\mathbf{y} - H(\bar{\boldsymbol{x}}^a))^2}$), broken down by time and by observation type. Each point plotted in Fig. S1 is the RMSE computed from all available global observations. This RMSE appears comparable in magnitude to several existing weather reanalysis products. For example, these statistics are similar to CAM-LETKF simulations by Liu et al. (2011), though simulations in that paper cover a much shorter time period. Furthermore, the temperature, pressure, and wind errors reported here are in the range of those listed for North American Regional Reanalysis (NARR) and ERA-Interim reanalysis (Mesinger et al., 2006; Dee et al., 2011).

The remainder of this section discusses the estimated covariance matrix parameters. These estimated parameters dictate both the variance of the model ensemble and the nugget variance. To that end, Fig. S2 displays a map of the average variance inflation factors in the model surface layer for February and July, 2009, and Fig. S3 shows how the average variance inflation factor changes over time through five months of CAM–LETKF simulations.

These figures show several notable patterns, three of which we discuss in more detail. First, the inflation factors in Fig. S2 are highest over North America, Asia, and Australia, regions with relatively abundant meteorological observations. A number of previous studies confirm this positive correlation between data density and covariance inflation (e.g., Anderson, 2009; Miyoshi, 2011; Miyoshi and Kunii, 2012). Furthermore, Miyoshi (2011) points out that a high inflation factor in observation-rich regions may cause the ensemble spread to be too large downwind. This explanation may account for the adjacent regions of high inflation (over continents) and low inflation (over the oceans) in Fig. S2. Second, the inflation factors are consistently low over eastern, tropical Pacific Ocean. This feature is intentional by design; we manually set inflation factors at a value of 0.4 in this region. Higher inflation values cause the ensemble variance to increase rapidly in this region and lead to unphysical temperature estimates near the tropopause. Third, the global average of the inflation factors is less than one (Fig. S3). Even though the inflation factors, on average, decrease the ensemble variance, the global ensemble variance remains relatively constant over time. For example, the average 6-hourly model ensemble spread at meteorology observation sites is comparable in February, June, and July: $\sim$1.5 m s^{-1} for zonal and meridional wind (standard deviation, square root of the averaged variances), $\sim$0.7 K for surface temperature, and $\sim$1.1 mb for surface pressure. This consistency, in spite of the small inflation average, may be due to the nonlinear nature of the meteorological model – differences among individual ensemble members can escalate or intensify over the 6-hour meteorology forecast.

In addition to the covariance inflation, the nugget variance also remains consistent over time. Fig. S4 shows the square root of the nugget variance for each observation type and at each model time period. Note that we estimate different values of the nugget variances by observation type and time, but the estimated variances are spatially constant across the globe. These estimates remain consistent over time, except for the initial January spin-up period, during which the estimate slowly evolves from the initial guess.

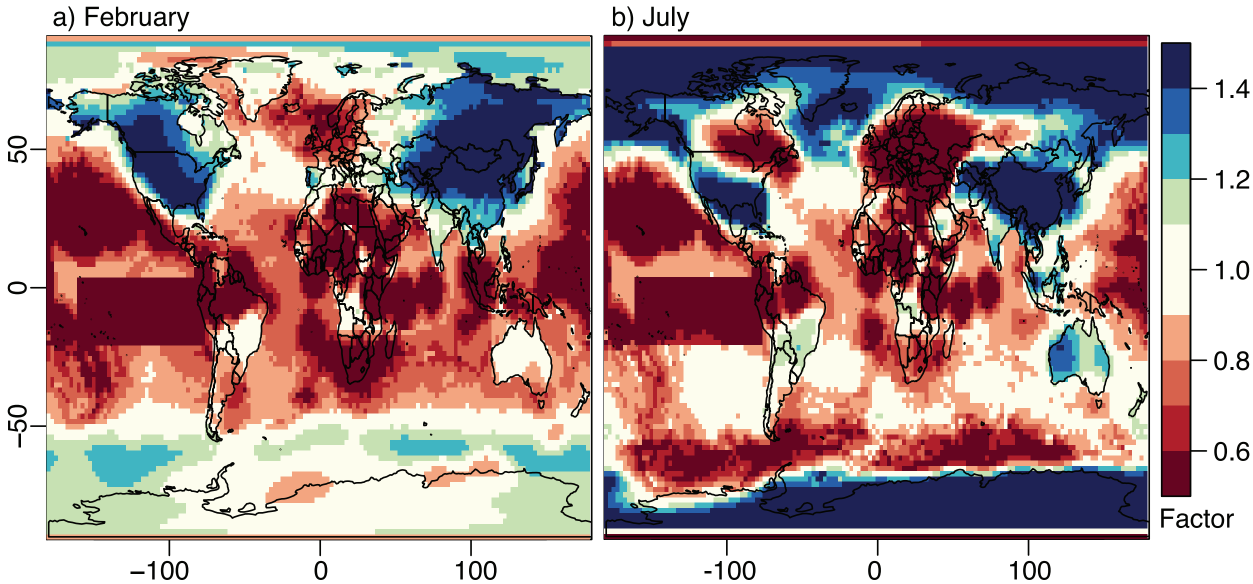

Figure S2: The variance inflation factors for the CAM model surface layer, averaged over each 6-hourly estimation period in February and July, 2009. In this study, we estimate a different inflation factor for each model grid box and each 6-hourly estimation period. More specifically, we estimate a single inflation factor for all model parameters (e.g., wind, temperature, surface pressure, and specific humidity) in each box.

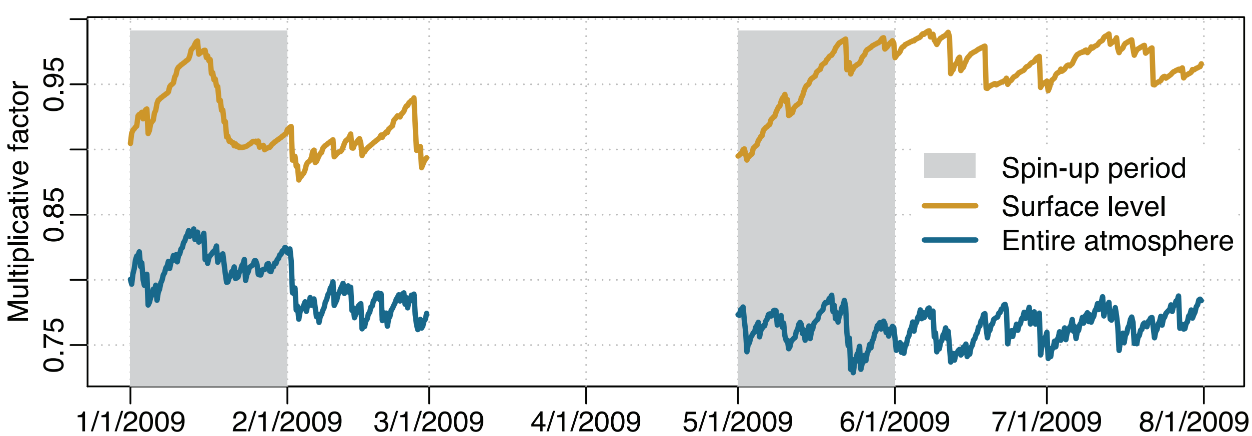

Figure S3: Time series of the average variance inflation factors, both at the surface and for all vertical model levels. The inflation factors show some variability during the model spin-up periods, then stabilize to relatively constant values.

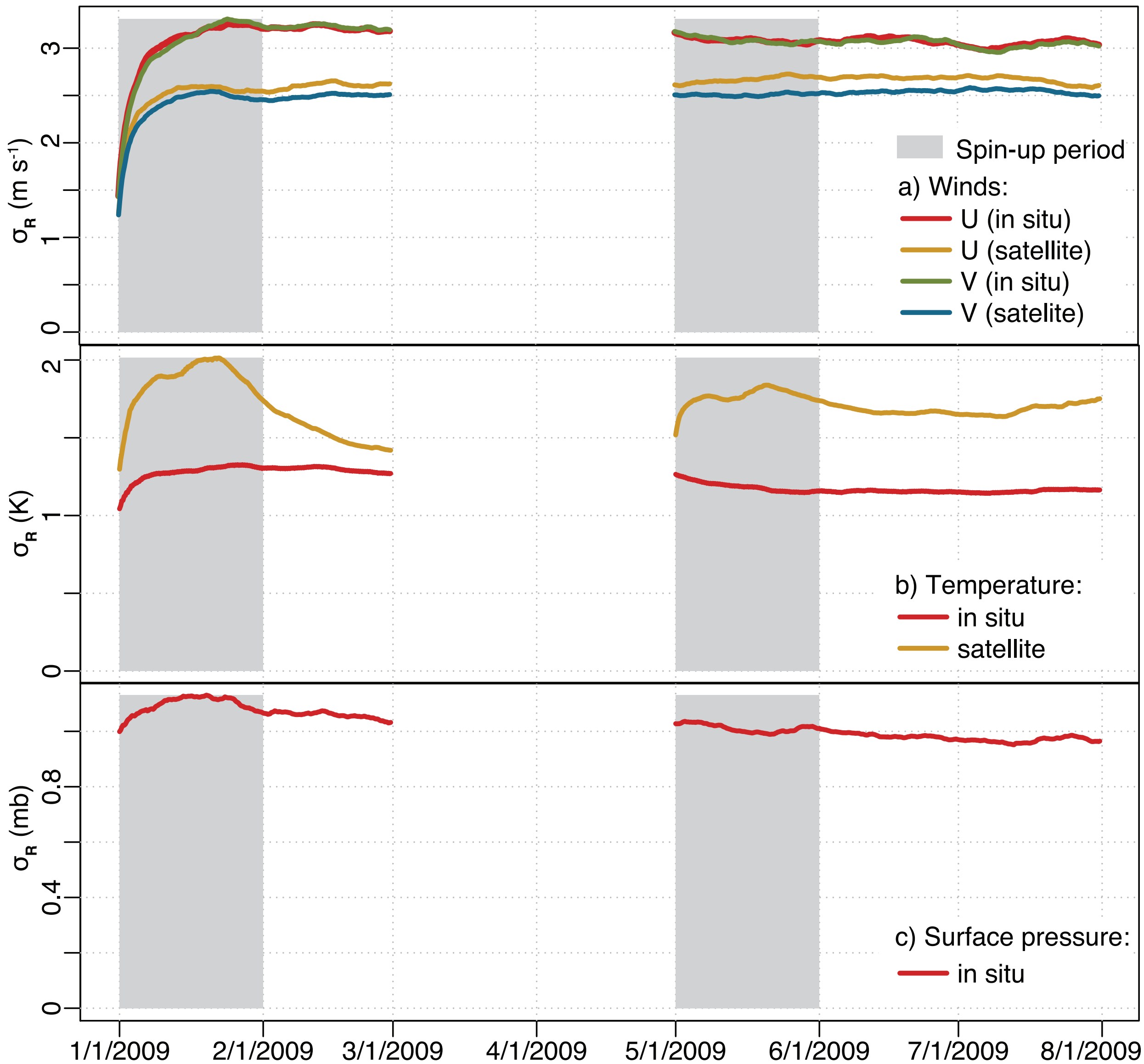

Figure S4: The square root of the nugget variance ($\sigma^2_{\mathbf{R}}$) estimated within CAM–LETKF.

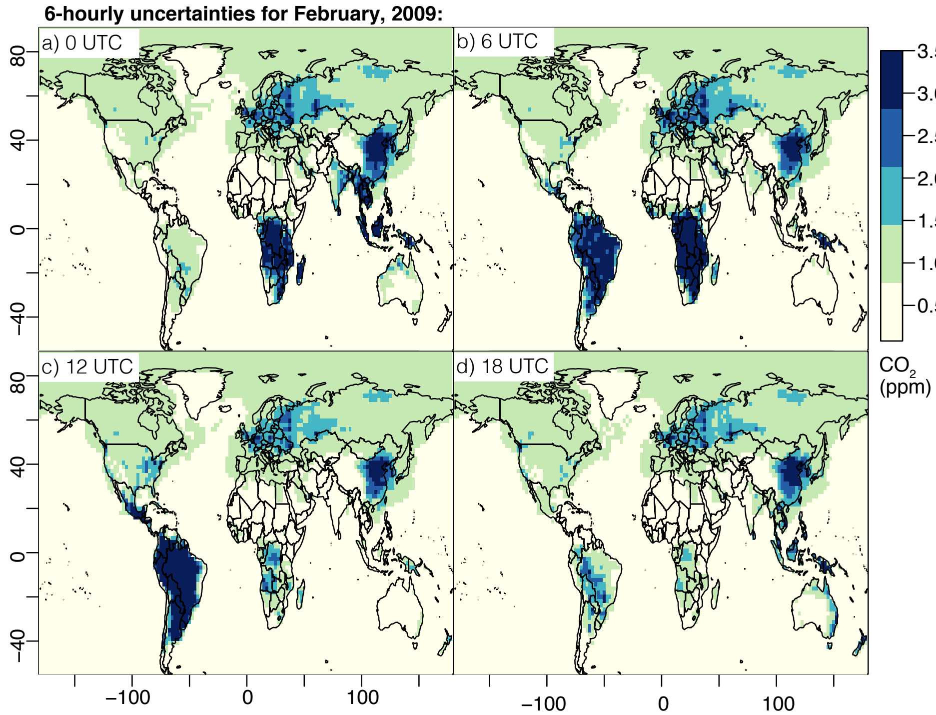

Figure S5: This figure displays the average 6-hourly CO_2 transport uncertainties in the model surface layer for a) 0 UTC, b) 6 UTC, c) 12 UTC, and d) 18 UTC. This figure is similar to Figs. 2a and 2b in the main manuscript except the uncertainties (standard deviations) shown here are disaggregated by time of day.

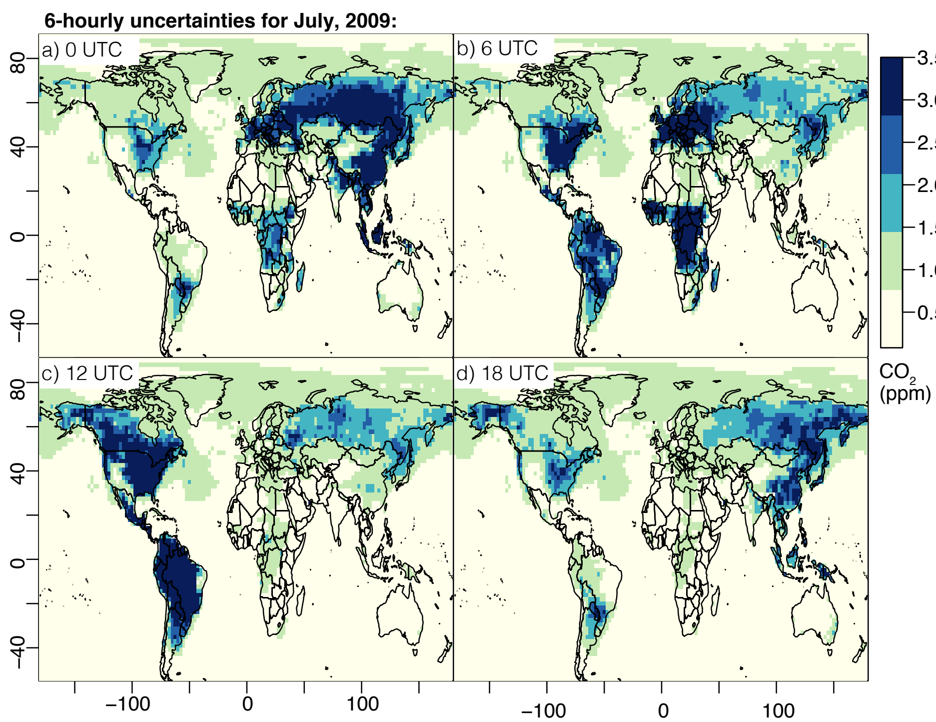

Figure S6: The CO_2 transport uncertainties for July, 2009, analogous to Fig. S5 but for a different time period.

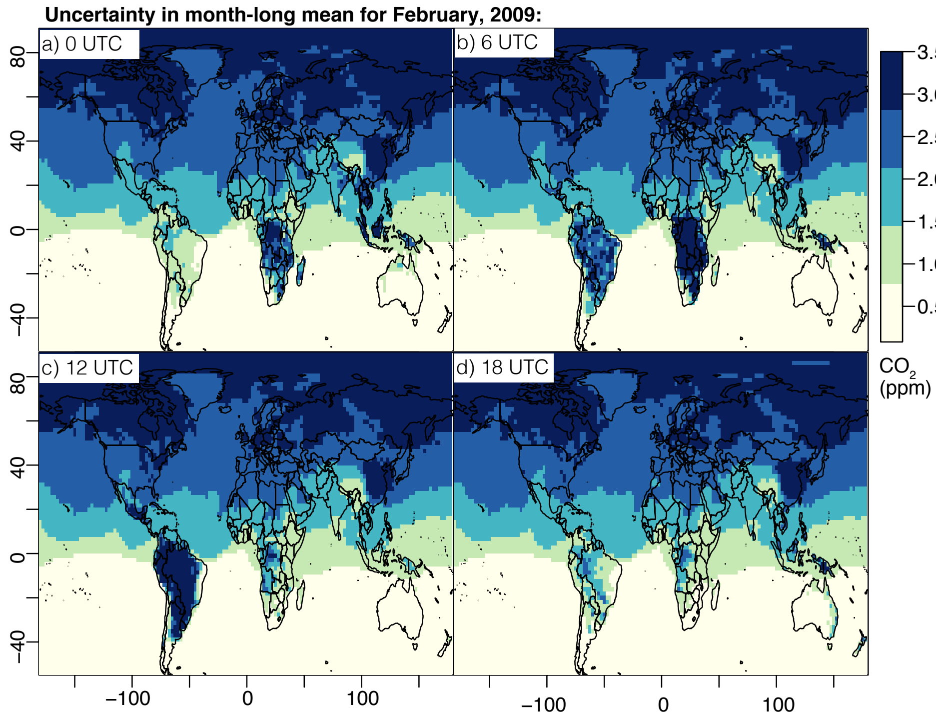

Figure S7: Uncertainties (standard deviations) in the monthly-averaged surface CO_2 concentrations for February, 2009. This figure is similar to Figs. 2c and 2d in the main article except the uncertainties are broken down by time of day for a) 0 UTC, b) 6 UTC, c) 12 UTC, and d) 18 UTC.

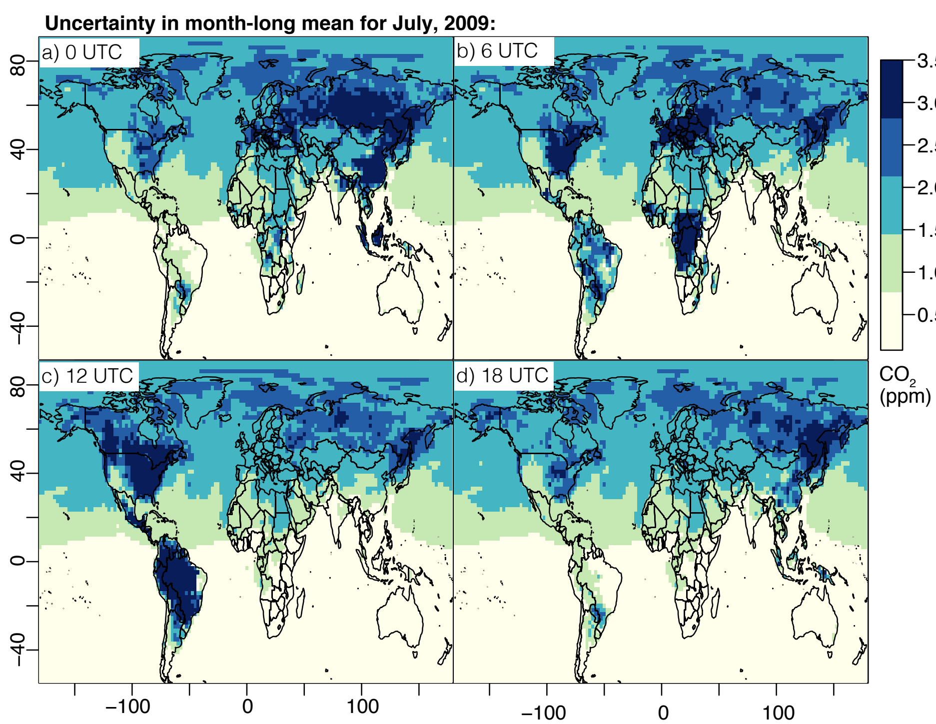

Figure S8: Uncertainties in the monthly-averaged surface CO_2 concentrations for July, 2009.

S3 Uncertainties in atmospheric CO_2 transport

This section of the supplement provides more detailed plots of the CO_2 transport uncertainties shown in Fig. 2 of the main article. In particular, the plots in this section (Figs. S5 – S8) visualize the transport uncertainties for different time slices of the day and show how CO_2 transport uncertainties differ between day and nighttime. The first two figures (Figs. S5 and S6) display the mean 6-hour CO_2 transport uncertainties for February and July, 2009, a setup analogous to Figs. 2a and 2b in the main manuscript. Conversely, Figs. S7 and S8 exhibit the uncertainties (standard deviations) in the month-long mean CO_2 concentrations, analogous to Figs. 2c and 2d in the main article.

In general, the 6-hourly uncertainties vary widely depending on the local time with higher uncertainties at night (Figs. S5 and S6). Note that the hypothesis test in the main article (sections 2.4 and 3.3) only uses model output associated with local afternoon CO_2 measurements. In contrast to these 6-hourly uncertainties, the uncertainties in monthly-mean concentrations do not vary as much by time of day (Figs. S7 and S8). For example, over North America and northern Eurasia in February, the CO_2 uncertainties are equally high during all times of day. However, a diurnal cycle in the month-long uncertainties is apparent over some regions – equatorial Africa, South America, and over Northern Hemisphere land regions in summer.

S4 CO_2 model-data comparisons

In this portion of the supplement, we show several CO_2 model and data time series from different types of observation sites (Figs. S9 – S14). These plots illustrate the capacity of CAM–LETKF (paired with Carbon Tracker fluxes) to reproduce hourly-averaged CO_2 observations. Furthermore, the plots provide greater context on the CO_2 ensemble spread and the estimated contribution of regional fluxes. The top panel of each figure illustrates the ensemble mean and ensemble spread, and the bottom panel shows the estimated contribution from regional fluxes – modeled CO_2 at the observation site minus modeled concentrations at 600 hPa. This increment is used for the hypothesis test in the main paper (section 2.4). In general, the modeled contribution of regional fluxes is largest during summer where biosphere uptake is strongest (e.g., LEF and AMT).

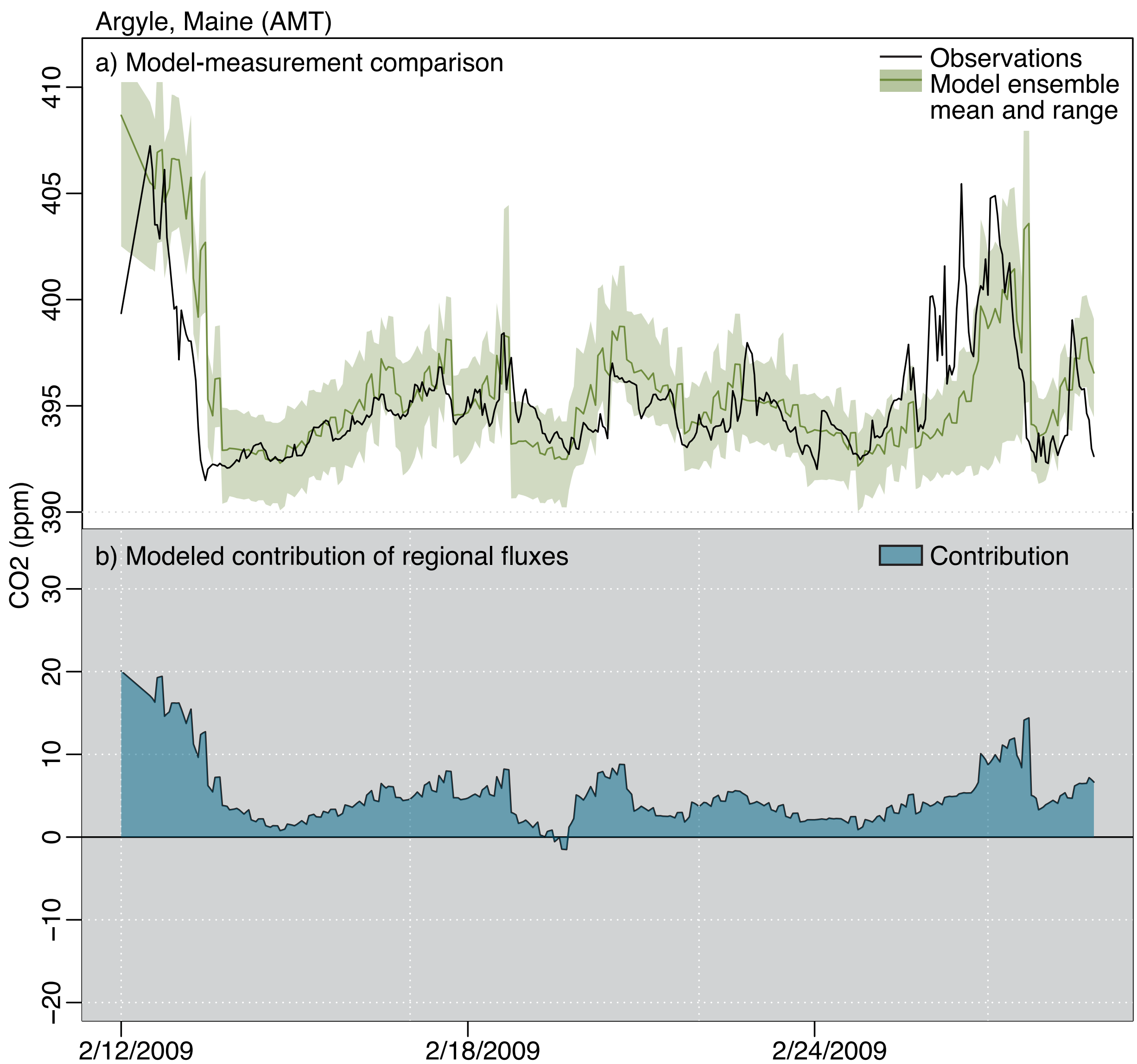

Figure S9: Panel (a) displays the hourly-averaged CO_2 measurements at Argyle tower, Maine, and the modeled CO_2 time series using CAM–LETKF and Carbon Tracker fluxes. Panel (b) shows the estimated contribution of regional CO_2 fluxes at the observation site. Here, we define this contribution as modeled CO_2 at the surface minus modeled CO_2 at 600 hPa.

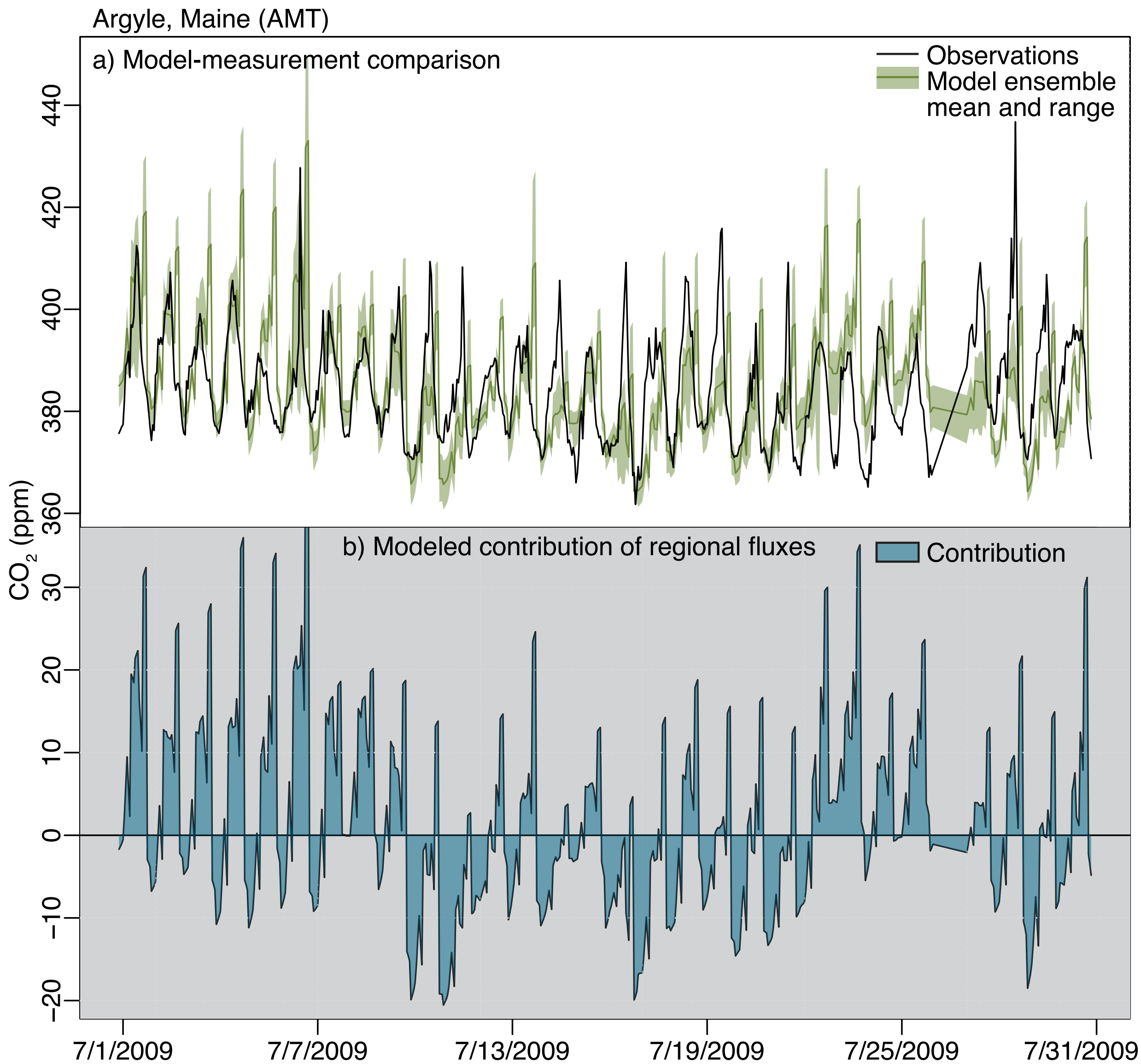

Figure S10: This figure is analogous to Fig. S9 but the Argyle tower in July 2009. Note that the top panel of each time-series plot (Figs. S9a– S14a) has a different y-axis, but the bottom panels (Figs. S9b– S14b) all have the same y–axis.

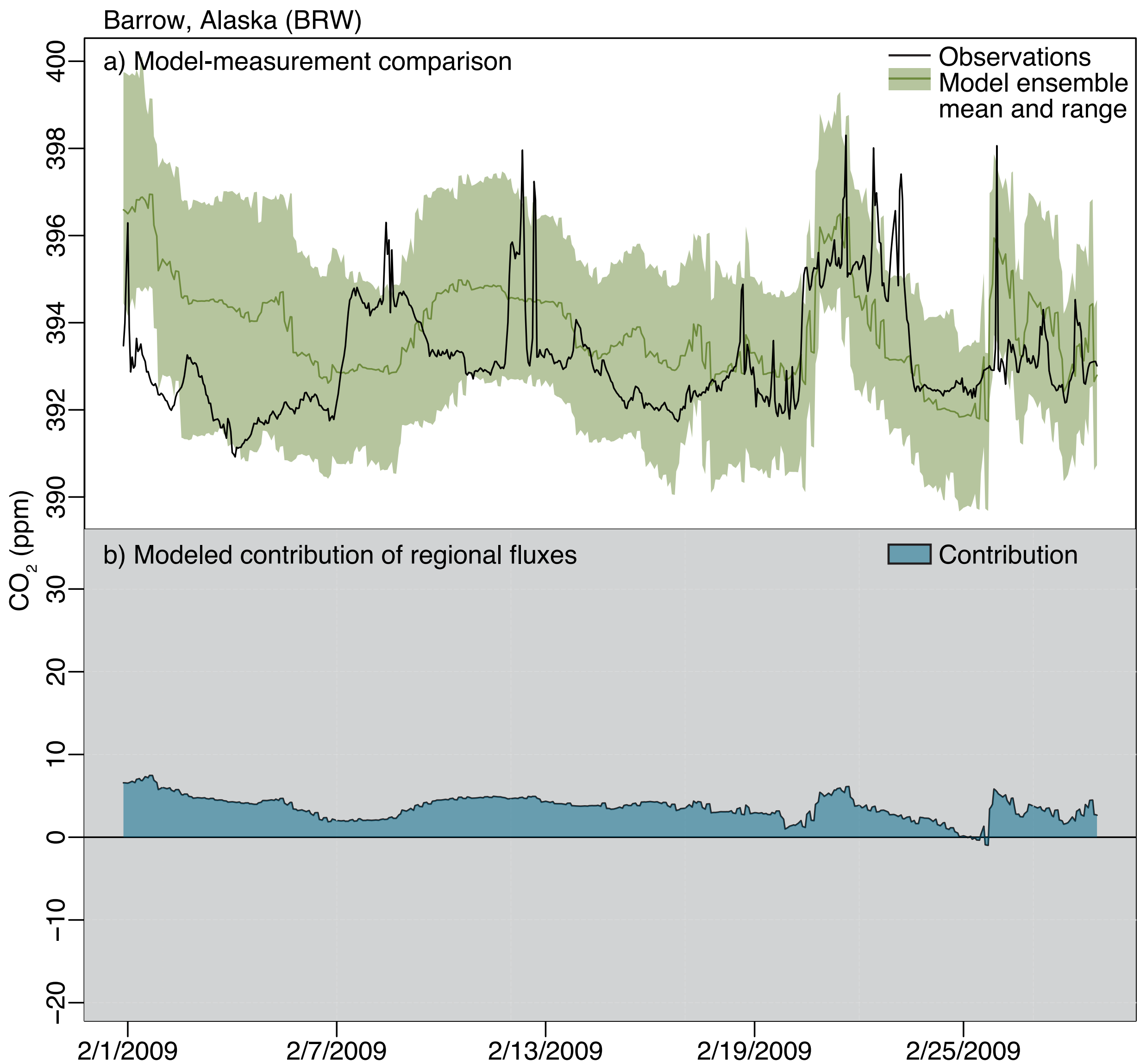

Figure S11: This figure is analogous to Fig. S9 but the Barrow, Alaska, in February 2009.

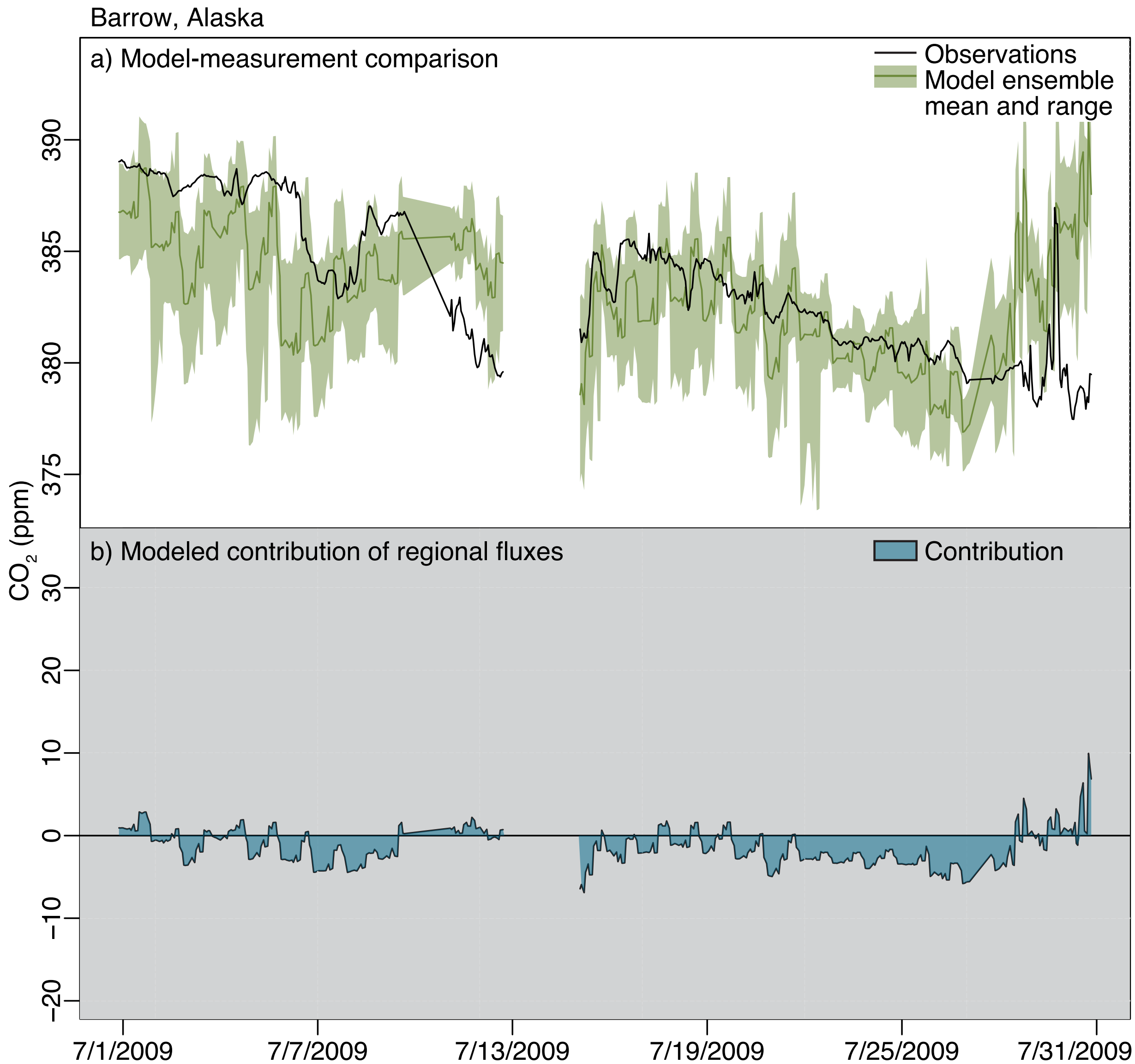

Figure S12: This figure is analogous to Fig. S9 but the Barrow, Alaska, in July 2009.

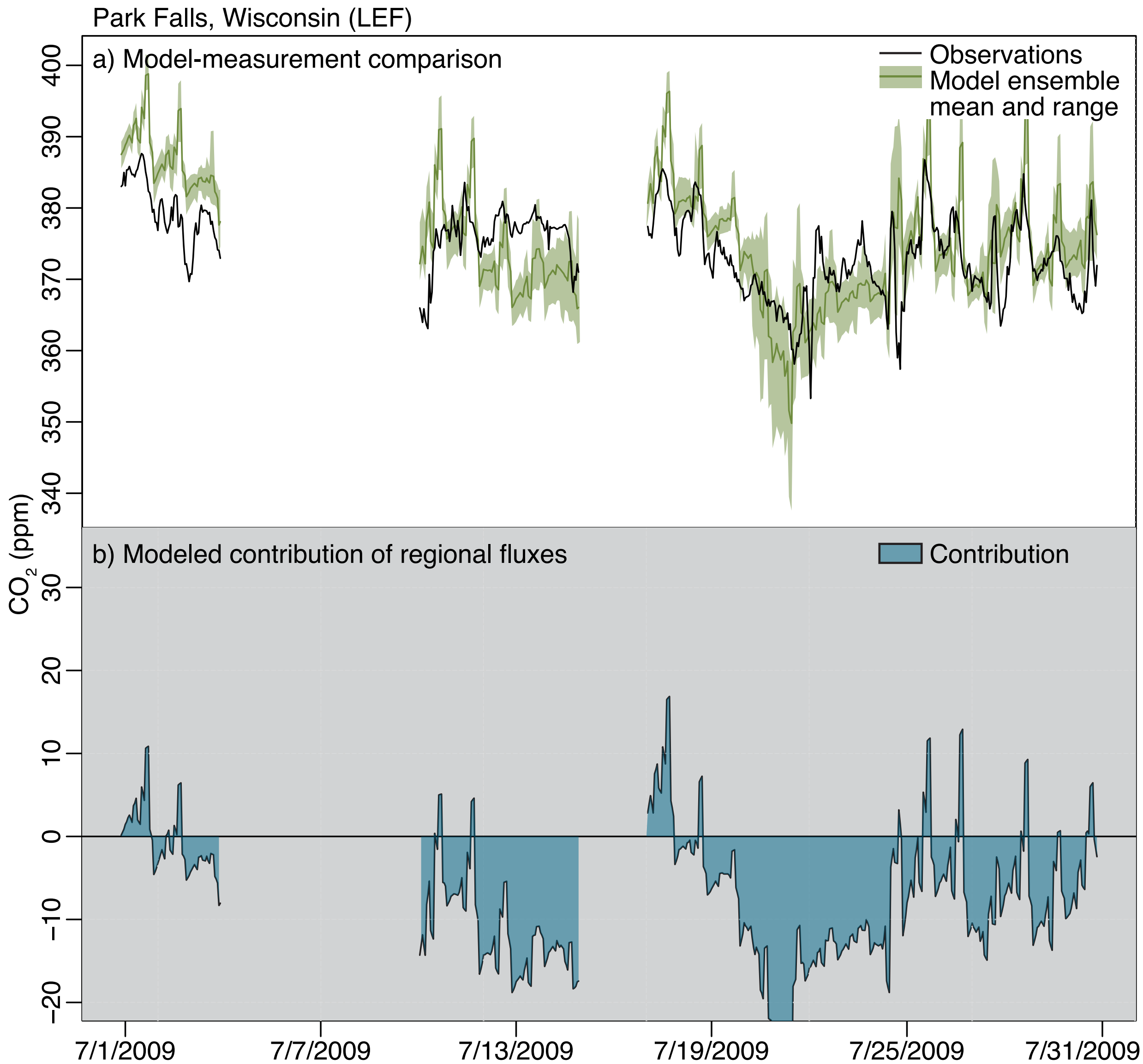

Figure S13: This figure is analogous to Fig. S9 but for the Wisconsin tall tower in July 2009.

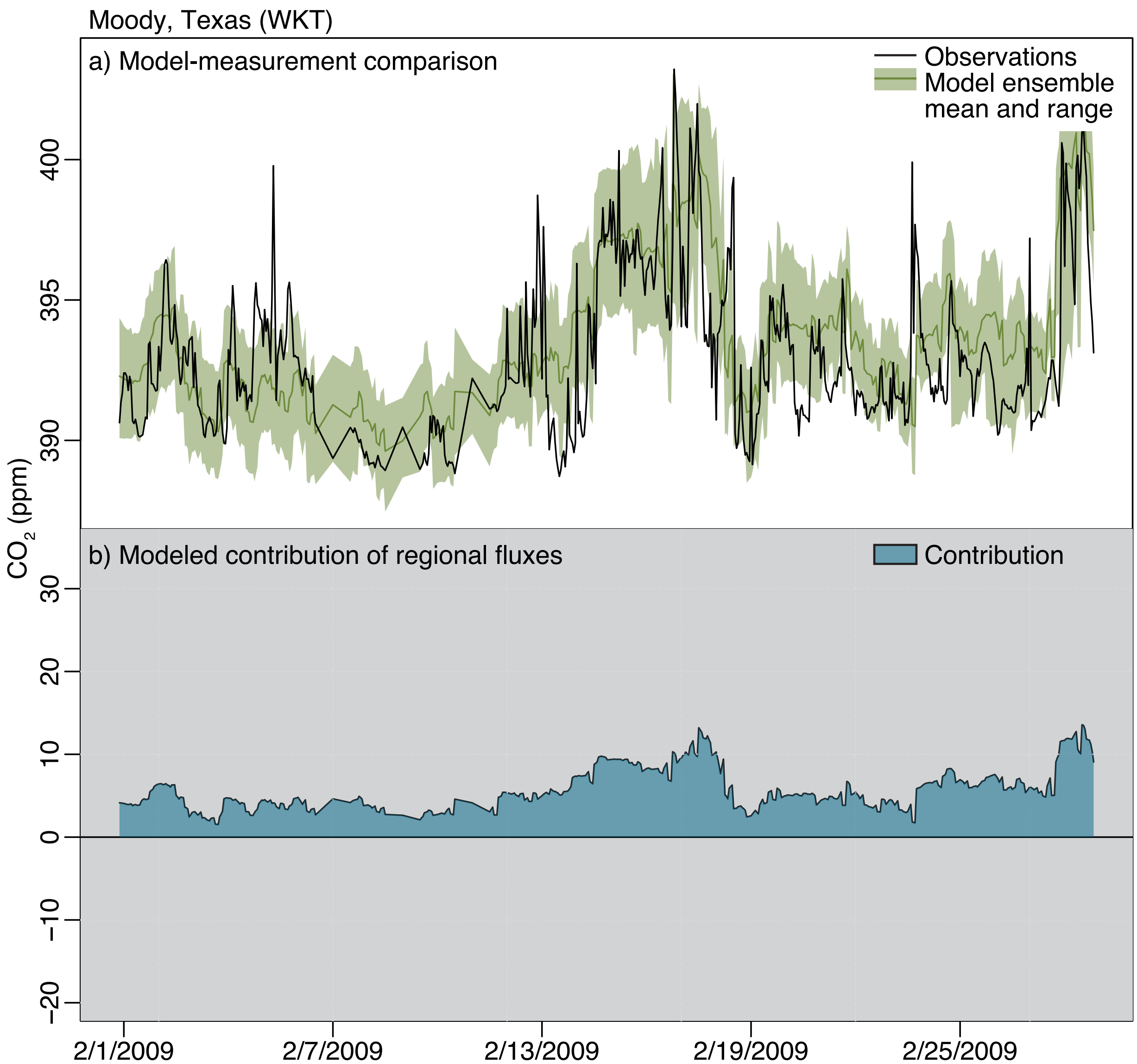

Figure S14: This figure is analogous to Fig. S9 but for the Texas tall tower in February 2009.

S5 Details of the variogram analysis

Section 3.2 of the main article describes the results of a variogram analysis of the CO_2 transport errors. The present section describes the methodology behind this analysis. We first construct a raw variogram using the CO_2 ensemble perturbations ($\mathbf{X}_{[CO_2]}$). The variogram describes the similarity between two perturbations at different time points (e.g., Kitanidis, 1997):

$$\gamma(\Delta t) \ = \ \frac{1}{2}\left(X_i(t_1) - X_i(t_2)\right)^2 \tag{S11}$$

where $X_i(t_1)$ refers to the perturbation of the i^{th} ensemble member at an individual location at time t_1 and $X_i(t_2)$ the perturbation from the same ensemble member and geographic location at time t_2. For each realization, we compute the raw variogram for all possible pairs of model outputs at a given location during the month of interest. Note that, in this setup, we only use model output associated with afternoon CO_2 observations (1pm – 7pm local time). We then bin the calculated values (from all realizations) based upon Δt and find the mean value of γ for all pairs in a given bin. The resulting, binned values of γ are called the empirical variogram.

Next, we fit a variogram model to the empirical variogram estimated above. In this case, we fit an exponential model:

$$\gamma(\Delta t) \ = \ \begin{cases} 0 & \text{if } \Delta t = 0 \\ \tau^2 + \sigma^2\left(1 - \exp\left(-\frac{\Delta t}{d}\right)\right) & \text{if } \Delta t > 0 \end{cases} \tag{S12}$$

where σ^2 is the variance of the perturbations at large separation times and d is the e-folding decorrelation time of the perturbations. Note that the total error decorrelation time is approximately $3d$. Furthermore, τ^2 is the nugget variance, error variance that is not correlated in time. Refer to Kitanidis (1997) for more detail on constructing and fitting variogram models.

The tables in this section (Tables S1a and S1b) display the results of the variogram analysis – the individual variogram parameters fitted at each individual CO_2 observation site. For more discussion of these parameters, refer to section 3.2 of the main article.

Table S1a: Fitted variogram parameters by site for Feb. 2009

Site	τ^2 (ppm^2)	σ^2 (ppm^2)	$3d$ (days)
AMY	0.32	3.14	4.18
GSN	0	2.85	3
RYO	0	0.28	1.93
YON	0	0.64	3.91
IZO	0	0.05	4.16
MHD	0	0.23	1.09
HEI	0	3.57	1.13
HUN	0	1.47	1.38
LMU	0	0.5	1.59
NOR	0	1.4	2.13
PAL	0	0.86	1.99
BIK	0	1.71	2.64
CBW	0	5.22	1.13
OXK	0	0.41	1.58
TRN	0	2.79	1.45
TTA	0	0.2	1.02
BRW	0	0.18	2.16
WSA	0.06	0.22	2.95
AMT	0	0.31	1.85
CHM	0	0.21	2.66
ETL	0	0.25	3.03
FSD	0	0.28	1.97
SGP	0	0.62	2.19
BAO	0	0.4	1.32
LEF	0	0.32	2.06
WBI	0	0.39	1.78
WKT	0	0.47	1.88
mean	0.01	1.1	2.2

Table S1b: Fitted variogram parameters by site for Jul. 2009

Site	τ^2 (ppm^2)	σ^2 (ppm^2)	$3d$ (days)
AMY	0.01	1.62	2.25
GSN	0	0.83	4.33
RYO	0	1.15	3.3
YON	0	0.09	1.81
IZO	0	0.05	4.54
MHD	0	0.32	1.47
HEI	0	0.41	1.55
HUN	0	0.8	2.08
LMU	0	0.15	1.97
NOR	0	0.35	1.71
PAL	0	0.53	1.73
BIK	0	0.73	2.01
CBW	0	0.57	1.59
OXK	0	0.38	2.14
TRN	0	0.4	1.92
TTA	0	0.25	1.84
BRW	0	1.01	1.9
WSA	0	1.65	2.02
AMT	0	1.44	2.68
CHM	NA	NA	NA
ETL	0	1.58	3.24
FSD	0	1.84	1.58
SGP	0	2.31	1.94
BAO	0	0.43	2.25
LEF	0	2.9	2.42
WBI	0	4.2	1.85
WKT	0	1.71	2.49
mean	0	1.1	2.3

S6 Statistical discussion of case study 1

This section of the supplement provides more in depth discussion of the theoretical aspects of the hypothesis test in case study 1. The outcomes of this hypothesis test hinge both on the variance of the CO_2 transport errors but also upon any temporal correlation in those errors. This section illustrates the idea using theoretical distributions (Fig. S15).

The hypothesis test in case study 1 (section 2.4) of the main article tests whether hypothetical biases in Carbon Tracker CO_2 fluxes would be detectable above errors in CO_2 transport. In other words, the null hypothesis states that a hypothetical bias in the CO_2 fluxes is indistinguishable from the CO_2 transport errors. As discussed in section 2.4 of the main article, the $\boldsymbol{SSR}$ ($k \times 1$), or sum of squared CO_2 transport residuals associated with each ensemble member, will not be identical. Rather, the $\boldsymbol{SSR}$ will fall on a distribution because some ensemble members will be closer to the best estimate ($\bar{\boldsymbol{x}}_{[CO_2]}$) than others. In order to reject this null hypothesis, the flux bias ($FSSR$, Eq. 5) must lie within the upper 5% tail of the $\boldsymbol{SSR}$.

Figure S15 depicts the distribution of $\boldsymbol{SSR}$ for various scenarios where the CO_2 transport residuals have pre-defined, hypothetical characteristics. This plot helps visualize how changes in the CO_2 transport residuals would affect the results of the hypothesis test. We construct the plot as follows:

1. Define a set of hypothetical qualities for the CO_2 transport errors. We will define these errors as having a multivariate normal distribution with a mean of zero. In particular, define the standard deviation of the 6-hourly errors (σ) and the temporal correlation parameter (d, Eq. S12).

2. Generate a set of random numbers based based upon the parameters defined above. In this case, we generate 670 random numbers, a plausible number of afternoon-only CO_2 observations at a given observation site in one month. These random numbers represent hypothetical CO_2 transport errors with characteristics σ and d. These errors could, in theory, be generated by an individual ensemble member in CAM–LETKF and could represent one column of the matrix $\mathbf{X}_{[CO_2]}$ (see Eq. 1 of the main article).

3. Calculate the sum of squares for this randomly-generated vector of numbers. Record this value.

4. Repeat steps 2–3 thousands of times. As noted above, the SSR from each iteration will not be identical.

5. Collect the SSR from all iterations and plot them on a histogram.

The distributions in Fig. S15 illustrate how different types of CO_2 transport errors will influence the hypothesis test results. If the standard deviation of the errors increase, then the entire distribution of $\boldsymbol{SSR}$ will also shift to larger values. In that case, a given surface flux signal ($FSSR$) would need to be relatively large to be distinguishable above the model transport errors. Concomitantly, if the error correlation increases, some of the ensemble members (i.e., individual elements of $\boldsymbol{SSR}$) will consistently remain further from the ensemble mean. Those members will have a high SSR, skewing the entire distribution of $\boldsymbol{SSR}$ further to the right. In this circumstance, the surface CO_2 flux signal would also need to be relatively large to be distinguishable above atmospheric CO_2 transport errors. In summary, the atmospheric CO_2 observations are less sensitive to bias in the flux estimate both as the standard deviation and temporal correlations of the CO_2 transport errors increase.

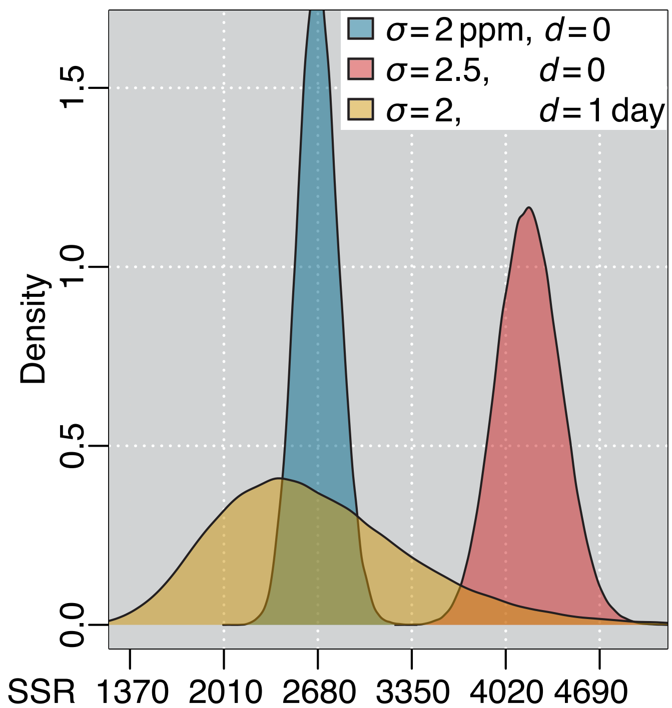

Figure S15: This figure shows the distribution of sum of squared residuals ($\boldsymbol{SSR}$) for hypothetical model ensembles with different characteristic residuals. It illustrates how different CO_2 transport errors would affect the results of the hypothesis test in case study 1; as the distribution of $\boldsymbol{SSR}$ reach higher and higher values, any biases in the estimated CO_2 fluxes ($FSSR$) become increasingly difficult to distinguish above the transport errors.

S7 Plots of meteorological variables and uncertainties (case study 2)

This section describes, in greater detail, the monthly-averaged meteorological parameters considered in the synthetic tracer experiment (sections 2.5 and 3.4). Table S2 lists all of the meteorological parameters that we compare against the synthetic tracer CV. We compare the synthetic tracer against the monthly-averaged meteorological parameters, the standard deviation in the monthly mean parameters, and the CV of each meteorological parameter – 60 parameters in total. Of those 60 parameters, 7 showed a correlation (R^2) with the tracer CV that is greater than or equal to 0.3. Figures S16 and S17 map these monthly-averaged, modeled meteorological parameters. Note that we do not include the oceans or Antarctica in the synthetic tracer study (Sections 2.5 and 3.4, Fig. 5 and 6). In general, those regions have small hourly CO_2 fluxes compared to other regions and do not contain many continuous CO_2 observation sites.

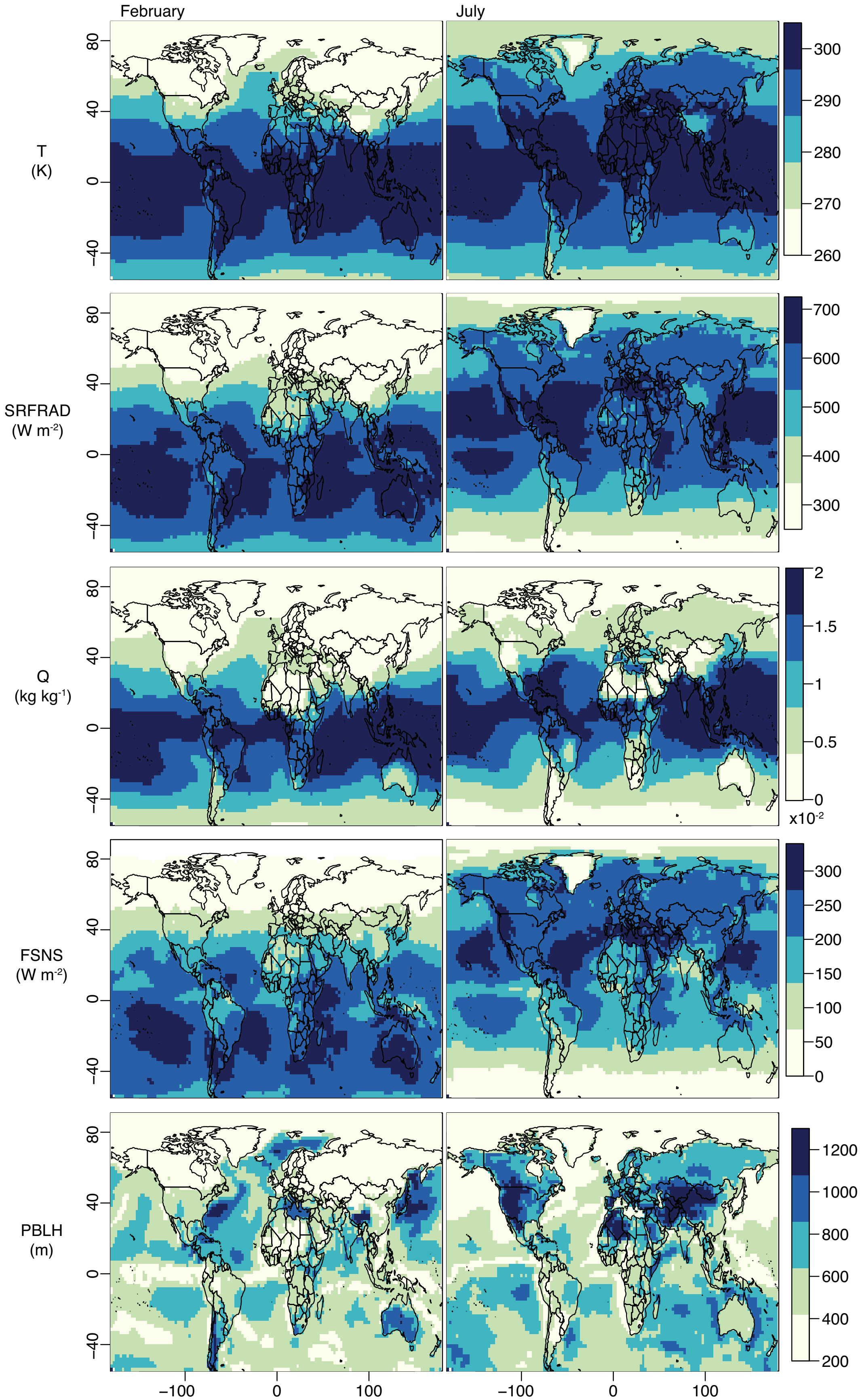

Figure S16: Maps of the monthly-averaged meteorological parameters from Fig. 6.

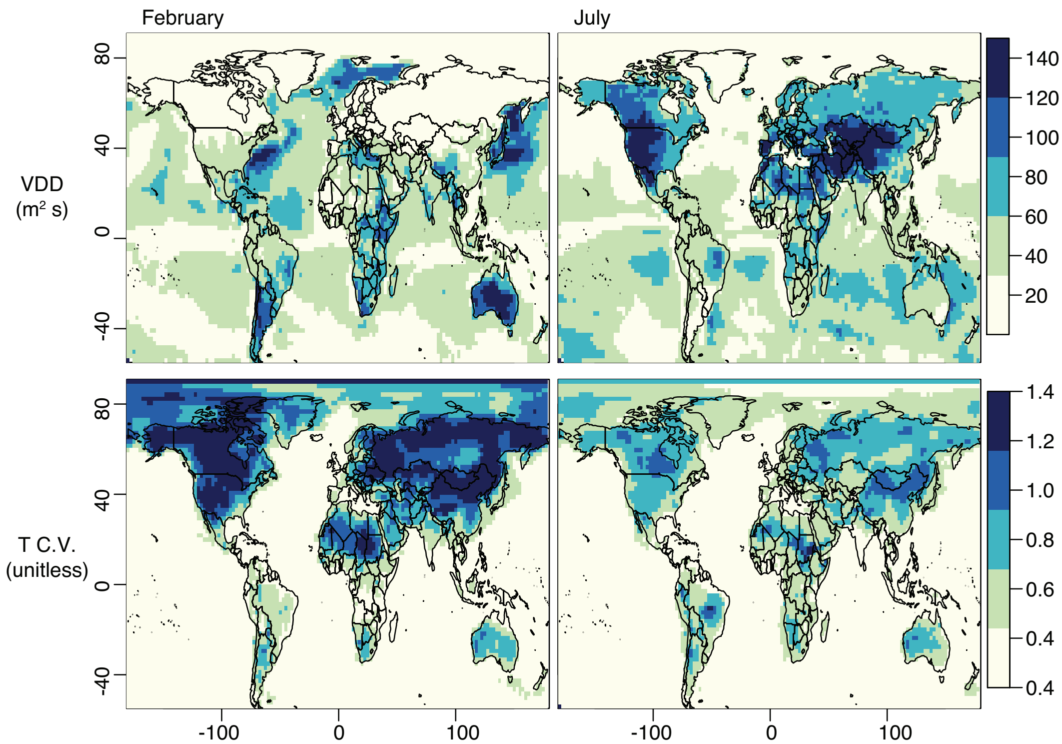

Figure S17: Maps of the monthly-averaged meteorological parameters from Fig. 6.

Table S2: Candidate meteorological variables

Meteorological variable	Abbreviation	Units
Zonal wind	U	m s^{-1}
Meridional wind	V	m s^{-1}
Total wind velocity	wind	m s^{-1}
Temperature	T	K
Planetary boundary layer height	PBLH	m
Vertical velocity	omega	Pa s^{-1}
Vertical velocity at 510hPa	omega510	Pa s^{-1}
Vertical diffusion diffusivity	VDD	m^2 s
Net longwave flux at the surface	FLNS	W m^{-2}
Surface sensible heat flux	SHFLX	W m^{-2}
Surface latent heat flux	LHFLX	W m^{-2}
Downwelling solar flux at surface	FSDS	W m^{-2}
Net solar flux at surface	FSNS	W m^{-2}
Solar flux reflected from surface	FSRS	W m^{-2}
Net radiative flux at surface	SRFRAD	W m^{-2}
Liquid cloud water	LCWAT	kg kg^{-1}
Relative humidity	RELHUM	%
Specific humidity	Q	kg kg^{-1}
Large-scale, stable precipitation rate	PRECL	m s^{-1}
Convective precipitation rate	PRECC	m s^{-1}

References

Anderson, J. L.: Spatially and temporally varying adaptive covariance inflation for ensemble filters, Tellus A, 61, 72–83, doi:10.1111/j.1600-0870.2008.00361.x, 2009.

Dee, D. P., Uppala, S. M., Simmons, A. J., Berrisford, P., Poli, P., Kobayashi, S., Andrae, U., Balmaseda, M. A., Balsamo, G., Bauer, P., Bechtold, P., Beljaars, A. C. M., van de Berg, L., Bidlot, J., Bormann, N., Delsol, C., Dragani, R., Fuentes, M., Geer, A. J., Haimberger, L., Healy, S. B., Hersbach, H., Hólm, E. V., Isaksen, L., Kållberg, P., Köhler, M., Matricardi, M., McNally, A. P., Monge-Sanz, B. M., Morcrette, J.-J., Park, B.-K., Peubey, C., de Rosnay, P., Tavolato, C., Thépaut, J.-N., and Vitart, F.: The ERA-Interim reanalysis: configuration and performance of the data assimilation system, Quarterly Journal of the Royal Meteorological Society, 137, 553–597, doi:10.1002/qj.828, 2011.

Desroziers, G., Berre, L., Chapnik, B., and Poli, P.: Diagnosis of observation, background and analysis-error statistics in observation space, Quarterly Journal of the Royal Meteorological Society, 131, 3385–3396, doi:10.1256/qj.05.108, 2005.

Hunt, B. R., Kalnay, E., Kostelich, E. J., Ott, E., Patil, D. J., Sauer, T., Szunyogh, I., Yorke, J. A., and Zimin, A. V.: Four-dimensional ensemble Kalman filtering, Tellus A, 56, 273–277, doi:10.1111/j.1600-0870.2004.00066.x, 2004.

Hunt, B. R., Kostelich, E. J., and Szunyogh, I.: Efficient data assimilation for spatiotemporal chaos: A local ensemble transform Kalman filter, Physica D: Nonlinear Phenomena, 230, 112 – 126, doi:10.1016/j.physd.2006.11.008, 2007.

Kanamitsu, M., Ebisuzaki, W., Woollen, J., Yang, S.-K., Hnilo, J. J., Fiorino, M., and Potter, G. L.: NCEP–DOE AMIP-II Reanalysis (R-2), Bulletin of the American Meteorological Society, 83, 1631–1643, doi:10.1175/BAMS-83-11-1631, 2002.

Kitanidis, P. K.: Introduction to Geostatistics: Applications in Hydrogeology, Stanford-Cambridge program, Cambridge University Press, Cambridge, 1997.

Li, H., Kalnay, E., and Miyoshi, T.: Simultaneous estimation of covariance inflation and observation errors within an ensemble Kalman filter, Quarterly Journal of the Royal Meteorological Society, 135, 523–533, doi:10.1002/qj.371, 2009.

Liu, J., Fung, I., Kalnay, E., and Kang, J.-S.: CO_2 transport uncertainties from the uncertainties in meteorological fields, Geophys. Res. Lett., 38, L12808, doi:10.1029/2011GL047213, 2011.

Liu, J., Fung, I., Kalnay, E., Kang, J.-S., Olsen, E. T., and Chen, L.: Simultaneous assimilation of AIRS XCO_2 and meteorological observations in a carbon climate model with an ensemble Kalman filter, J. Geophys. Res.-Atmos., 117, D05309, doi:10.1029/2011JD016642, 2012.

Mesinger, F., DiMego, G., Kalnay, E., Mitchell, K., Shafran, P. C., Ebisuzaki, W., Jović, D., Woollen, J., Rogers, E., Berbery, E. H., Ek, M. B., Fan, Y., Grumbine, R., Higgins, W., Li, H., Lin, Y., Manikin, G., Parrish, D., and Shi, W.: North American Regional Reanalysis, Bulletin of the American Meteorological Society, 87, 343–360, doi:10.1175/BAMS-87-3-343, 2006.

Miyoshi, T.: The Gaussian Approach to Adaptive Covariance Inflation and Its Implementation with the Local Ensemble Transform Kalman Filter, Monthly Weather Review, 139, 1519–1535, doi:10.1175/2010MWR3570.1, 2011.

Miyoshi, T. and Kunii, M.: The Local Ensemble Transform Kalman Filter with the Weather Research and Forecasting Model: Experiments with Real Observations, Pure and Applied Geophysics, 169, 321–333, doi:10.1007/s00024-011-0373-4, 2012.